



RELATIVISTIC MEASUREMENTS FROM TIMING THE BINARY PULSAR PSR B1913+16

J. M. WEISBERG AND Y. HUANG

Department of Physics and Astronomy, Carleton College, Northfield, MN 55057, USA; jweisber@carleton.edu*Received 2016 January 19; revised 2016 April 20; accepted 2016 June 1; published 2016 September 21*

ABSTRACT

We present relativistic analyses of 9257 measurements of times-of-arrival from the first binary pulsar, PSR B1913+16, acquired over the last 35 years. The determination of the “Keplerian” orbital elements plus two relativistic terms completely characterizes the binary system, aside from an unknown rotation about the line of sight, leading to a determination of the masses of the pulsar and its companion: $1.438 \pm 0.001 M_{\odot}$ and $1.390 \pm 0.001 M_{\odot}$, respectively. In addition, the complete system characterization allows for the creation of relativistic gravitation test by comparing measured and predicted sizes of various relativistic phenomena. We find that the ratio of the observed orbital period decrease caused by gravitational wave damping (corrected by a kinematic term) to the general relativistic prediction is 0.9983 ± 0.0016 , thereby confirms the existence and strength of gravitational radiation as predicted by general relativity. For the first time in this system, we have also successfully measured the two parameters characterizing the Shapiro gravitational propagation delay, and found that their values are consistent with general relativistic predictions. For the first time in any system, we have also measured the relativistic shape correction to the elliptical orbit, δ_{θ} , although its intrinsic value is obscured by currently unquantified pulsar emission beam aberration. We have also marginally measured the time derivative of the projected semimajor axis, which, when improved in combination with beam aberration modeling from geodetic precession observations, should ultimately constrain the pulsar’s moment of inertia.

Key words: binaries: close – gravitation – gravitational waves – pulsars: individual (PSR B1913+16)

Supporting material: .tar.gz files

1. INTRODUCTION

Pulsar B1913+16 was the first binary pulsar discovered (Hulse & Taylor 1975). The system consists of two neutron stars (one is an observed pulsar) orbiting in a very tight, highly eccentric orbit, and it remains one of the best for studying relativistic gravitation (Weisberg & Taylor 1981; Taylor & Weisberg 1982, 1989; Weisberg et al. 2010, hereafter WNT). In this paper we update WNT with the addition of post-2006 data and with further relativistic timing analyses. The addition of significant quantities of data acquired with modern data-acquisition devices has enabled us to measure several additional relativistic phenomena for the first time in this system, while also refining previously measured ones. Among the parameters newly measured with various degrees of accuracy are the Shapiro gravitational propagation delay, a relativistic correction to the elliptical orbital shape, and the time derivative of projected pulsar semimajor axis. All of the data used in this study are published with this paper in a .tar.gz package and in two online repositories, while our analysis software is published on sourceforge.

We describe the observations used in this work in Section 2, while Section 3 delineates the scope and methods of our relativistic analyses of these data. The results of our fits to the data are explained in Section 4, and their applications for tests of relativistic gravitation are discussed in Section 5. We conclude in Section 6 by summarizing our work and placing it in the context of results from other relativistic binary pulsar systems.

2. DATA

The data for our analyses consists of 9257 pulse times-of-arrival (TOAs) derived from five-minute integrations of the pulsar signal at frequencies near 1400 MHz measured at Arecibo Observatory from 1981 to 2012. The parameters of

the various observing systems and the number of TOAs from each through epoch 2006 are tabulated in WNT; WAPP spectrometer observations since then have added another 1652 TOAs to the total, each acquired by three WAPPs deployed simultaneously at approximately contiguous 100 MHz bands near 1400 MHz.

Geodetic precession of the pulsar spin axis has induced pulse profile changes (Weisberg et al. 1989; Kramer 1998; Weisberg & Taylor 2002; Clifton & Weisberg 2008) that have lately grown increasingly larger, presumably as our line of sight approaches the edge of the pulsar beam. Nevertheless, for purposes of uniformity we use only a single profile template while finding TOAs for all WAPP data. This procedure induces time offsets into our TOA data set between different sessions and frequencies, which have grown to a level where they should be compensated for. To do so, we adopted the following process. First, we formed a pulse profile at each frequency band for each two-week session. Each resulting “session-band” standard profile has a much greater signal-to-noise ratio than does a single five-minute integration, while still being short enough to avoid the secular changes we are trying to measure. Next, we measured the offset of the midpoint of this session-band standard profile with respect to the grand standard profile. (The midpoint is assumed to correspond to a fixed longitude on the pulsar regardless of profile shifts).

Then we fitted out a “primary” linear model of the profile offsets as a function of time at each band. In this fashion, we provided an empirically determined, model independent, first-order TOA correction that accounts for the effects of profile changes, thereby minimizing the long-term effects of profile shifts that might be mistaken as the signature of other phenomena. We next fitted the timing model to all such “primarily offsetted” TOAs and chose the resulting dispersion measure as our nominal value. Finally, secondary offsets were

determined through single session fits, where the dispersion measure was fixed at its nominal value and the residual offset of each band was fitted for and then removed. This process ensures that the infinite-frequency TOAs calculated from each band and session are self-consistently de-dispersed¹ and offsetted.

To verify that the above profile variation correction process does not contaminate our parameter measurements, we also employed an alternate approach, fitting for an offset for each band in each session simultaneously with all other parameters (Demorest et al. 2013). This procedure yields parameters that agree with our method to within 1σ for all parameters, suggesting that our measurements are robust with respect to the methods used to remove profile-shift-induced timing offsets.

3. RELATIVISTIC ANALYSIS OF TOAS

Using an augmented version of the TEMPO software program, we fitted the relativistic timing model of Damour & Deruelle (1989, hereafter **DD**), or, in certain cases, the **DD** model augmented by the Freire & Wex (2010, hereafter **FW**) Shapiro parametrization (see Section 3.1),² to our TOAs. In these models, the pulsar signal encounters several distinct types of delays on its journey from the orbiting pulsar to the solar system barycenter, such that the infinite-frequency pulse arrival time at the solar system barycenter, t_{ssbc} , is given by

$$t_{\text{ssbc}} = D^{-1}[T + \Delta_{\text{Roemer}}(T) + \Delta_{\text{Einstein}}(T) + \Delta_{\text{Shapiro}}(T) + \Delta_{\text{Aberration}}(T)], \quad (1)$$

where each delay is a function of the pulsar proper time of pulse emission, T , and whose details depend on a number of physical parameters (The Doppler factor, D , accounts for the relative motion of the solar system and binary system barycenters) The various terms in Equation (1) are detailed in **DD** and Damour & Taylor (1992, hereafter **DT92**), and we will comment further on the last two terms of Equation (1) in the following two sections.

Among the fitted parameters, we determined improved values of the pulsar spin and orbital parameters that were published in **WNT**, plus a number of new ones. For the first time, we have successfully fitted for the Shapiro (1964) gravitational propagation delay while also placing constraints on two additional ones: a relativistic correction to the quasi-elliptical shape of the orbit, and the shrinkage rate of its projected semimajor axis, as described in further detail below.

The improved, previously fitted parameters include the pulsar spin frequency and derivative(s) f , \dot{f} , ... ; five ‘‘Keplerian’’ orbital elements defined as projected pulsar semimajor axis $x \equiv a_1 \sin i$ where i is the orbital inclination; orbital period, P_b ; eccentricity, e ; reference epoch, T_0 ; the reference epoch’s longitude of periastron, ω_0 ; relativistic ‘‘post-Keplerian’’ parameters defined as the mean rate of periastron advance $\langle \dot{\omega} \rangle$; gravitational redshift-time dilation term γ ; and orbital period derivative \dot{P}_b .

The newly fitted post-Keplerian parameters include the following: (i) two Shapiro delay terms called shape (s) and range (r) in the **DD** parametrization, or two (different) quantities, ζ and

h_3 , in the alternate **FW** parametrization; (ii) the orbital elliptical shape correction parameter $\delta_\theta^{\text{obs}}$ (to our knowledge never previously fitted for in any binary system), which appears in **DT92**’s full expression for Equation (1)’s Roemer term³; and (iii) \dot{x}^{obs} and \dot{e}^{obs} , the observed time derivatives of x and e . All of the new parameters are discussed in greater detail in Sections 3.1–3.3, while the fit results for both old and new parameters are described in Section 4, and relativistic tests resulting from these measurements are discussed in Section 5. A set of TEMPO input files containing input parameters and the TOAs is available in a .tar.gz package published with this paper, in a persistent repository <http://dx.doi.org/10.5281/zenodo.54764>, and with the article preprint <http://arxiv.org/e-print/1606.02744v1>.

3.1. Fitting for the Shapiro Gravitational Propagation Delay via Two Different Parametrizations

Until this work, we were unable to explicitly measure the two Shapiro gravitational propagation delay terms that characterize Equation (1)’s $\Delta_{\text{Shapiro}}(T)$, because of their relatively small timing signature and their covariance. The two terms are identified as s and r in **DD**, while **FW** recently developed an alternate parametrization of the phenomenon wherein their two fitted parameters, ζ and h_3 , are orthonormal. Our software implementation of their parametrization for high-eccentricity pulsars is available in our augmented version of TEMPO (see footnote 2).

The measurements of either pair of Shapiro parameters, (s , r) or (ζ , h_3), can be utilized in either of two different manners, as described below.

First, if general relativity is assumed to be the correct theory of gravitation, then either pair of Shapiro measurables can be utilized as independent constraints on the orbital inclination and binary companion mass. We summarize the theory here, and then apply it in Section 4.2.

In the **DD** formulation, s and r translate directly into $\sin i$ and m_2 (the companion mass), respectively

$$\sin i = s, \quad (2)$$

and

$$m_2 = \left(\frac{c^3}{G}\right) r = \left(\frac{r}{T_\odot}\right) M_\odot, \quad (3)$$

with c the speed of light, G as the Newtonian gravitational constant, $T_\odot = G M_\odot / c^3 = 4.925,490,947 \mu\text{s}$.

The alternate **FW** parametrization of the Shapiro delay gives

$$\sin i = \frac{2\zeta}{\zeta^2 + 1}, \quad (4)$$

while m_2 is a combination of the two measurables (h_3 , ζ)

$$m_2 = \left(\frac{c^3}{2G}\right) \frac{h_3}{\zeta^3} = \left(\frac{h_3/\zeta^3}{T_\odot}\right) M_\odot. \quad (5)$$

Alternatively, each measured parameter of the Shapiro pair can be considered to be an independent test of relativistic gravitation. We apply this procedure in Section 5.2.

¹ This procedure also absorbs TOA variations induced by DM fluctuations at the levels and timescales expected from studies of millisecond pulsars (You et al. 2007).

² See <http://sourceforge.net/projects/TEMPO/> for our augmented version of TEMPO, which contains our fitting routine for the **FW** Shapiro parameters in high-eccentricity binaries.

³ Before it can be utilized for tests of relativity, the $\delta_\theta^{\text{obs}}$ parameter must be corrected for a comparable aberration term which is currently undeterminable (see Section 4.4).

3.2. Determination of the Relativistic Orbital Shape Correction δ_θ in the Presence of the Aberration Delay

In order to successfully measure the intrinsic value of δ_θ , which nominally quantifies a relativistic correction to the shape of the approximately elliptical orbit in Equation (1)'s Roemer delay expression, one must compensate the observed value for the influence of a phenomenon that comparably affects TOAs, namely the orbital-phase dependent aberration of the pulsar beam as described by DD and DT92. Those authors provide a prescription for calculating and eliminating the confounding aberration signature from the observed value of δ_θ if the aberration geometry is known. In principle, the necessary information can be gleaned from studies of profile changes resulting from geodetic precession of the pulsar spin axis (Weisberg & Taylor 2002; Clifton & Weisberg 2008). In this section, we summarize the theoretical expressions required to quantify δ_θ and aberration, and we will apply our observations to these results in Section 4.4.

The time delay $\Delta_{\text{Aberration}}$ in Equation (1), resulting from aberration of the rotating pulsar beam, is dependent on the time-variable transverse component of the pulsar's orbital velocity. DD and DT92 parametrize the instantaneous delay via the aberration parameters $A(t)$ and $B(t)$

$$\Delta_{\text{Aberration}} = A(t) \{ \sin(\omega + A_e(u)) + e \sin \omega \} + B(t) \{ \cos(\omega + A_e(u)) + e \cos \omega \}, \quad (6)$$

where $A_e(u)$ is a true-anomaly like quantity, and $A(t)$ and $B(t)$ are dependent on the precessing spin-axis geometry

$$A(t) = -\frac{f^{-1}}{P_b} \frac{x}{\sin i (1 - e^2)^{1/2}} \frac{\sin \eta}{\sin \lambda}, \quad (7)$$

$$B(t) = -\frac{f^{-1}}{P_b} \frac{x}{\sin i (1 - e^2)^{1/2}} \frac{\cos i \cos \eta}{\sin \lambda}, \quad (8)$$

with λ and η the geodetically precessing polar angles of the pulsar spin axis with respect to the line of sight and line of nodes, respectively. (DD and DT92 suggested the substitution of a single fixed parameter, A_0 , for the two parameters $A(t)$ and $B(t)$ because observations at the time suggested that the spin and orbital angular momenta are aligned. However, subsequent observations of pulse profile changes have shown that this is not the case.)

While the above equations provide a complete description of the calculation of $\Delta_{\text{Aberration}}$ at any proper emission time, DD and DT92 also provide an alternate approach that focuses on aberration parameters that change slowly (on precession timescales) as a result of spin axis precession. This procedure, detailed below, is more closely tailored to parameters determinable from TOA analyses.

DT92 show that aberration will bias the observed value of the relativistic orbital shape parameter, $\delta_\theta^{\text{obs}}$, with respect to its intrinsic value, $\delta_\theta^{\text{intr}}$

$$\delta_\theta^{\text{obs}} = \delta_\theta^{\text{intr}} - \epsilon_A, \quad (9)$$

where the small parameter ϵ_A is defined as

$$\epsilon_A \equiv \frac{A(t)}{x}. \quad (10)$$

Hence the observational bias can be removed, given measurements of the aberration parameter $A(t)$ and the Keplerian

quantity x . The corrected value $\delta_\theta^{\text{intr}}$ could then serve as an additional test of gravitation theory.

3.3. Other Parameters Affected by the Aberration Delay

In addition to affecting δ_θ , DT92 show that aberration also affects the observed x and e values. However, the fractional corrections to x and e are tiny. More interesting is the effect of geodetic spin axis precession on the time-derivatives of these parameters, because DT92 show that they are potentially measurable. The precessional motion will cause the aberration geometry to change, resulting in secular changes to $A(t)$ and hence to ϵ_A on precession timescales

$$\frac{d\epsilon_A}{dt} = \frac{1}{x} \frac{dA(t)}{dt} = -\frac{f^{-1}}{P_b} \frac{1}{\sin i (1 - e^2)^{1/2}} \times \frac{\Omega_1^{\text{geodetic}}}{\sin^2 \lambda} (\sin i \cos \lambda \sin 2\eta + \cos i \sin \lambda \cos \eta), \quad (11)$$

where $2\pi/\Omega_1^{\text{geodetic}}$ is the geodetic precession period of the pulsar spin axis. The observed, normalized time derivative of e results from the sum of two phenomena

$$\left(\frac{\dot{e}}{e}\right)^{\text{obs}} = \frac{d\epsilon_A}{dt} + \left(\frac{\dot{e}}{e}\right)^{\text{GW}}, \quad (12)$$

where ‘‘GW’’ designates effects due to gravitational waves, while the observed, normalized time derivative of x stems from a combination of five terms:

$$\left(\frac{\dot{x}}{x}\right)^{\text{obs}} = \frac{d\epsilon_A}{dt} + \left(\frac{\dot{a}_1}{a_1}\right)^{\text{GW}} + \left(\cot i \frac{di}{dt}\right)^{\text{SO}} - \mu \cot i \sin(\Theta_\mu - \Omega) - \frac{\dot{D}}{D}, \quad (13)$$

where ‘‘SO’’ refers to spin-orbit coupling. (See Lorimer & Kramer 2004) for an expression that includes additional terms needed for some other binary pulsars.)

The quantity di/dt in the third term of Equation (13), resulting from pulsar spin-orbit coupling, is developed here, from expressions in DT92:

$$\begin{aligned} \frac{di}{dt} &= \frac{G}{c^2} \left\{ 2 + \frac{3 m_2}{2 m_1} \right\} \frac{S_1}{a_R^3 (1 - e^2)^{3/2}} \sin \lambda \cos \eta \\ &= \frac{1}{c^2} \left\{ 2 + \frac{3 m_2}{2 m_1} \right\} \frac{I_1 (2\pi f) (2\pi/P_b)^2}{(m_1 + m_2) (1 - e^2)^{3/2}} \sin \lambda \cos \eta, \end{aligned} \quad (14)$$

where m_1 is the pulsar mass, a_R is the semimajor axis of the relative orbit, $S_1 = I_1 (2\pi f)$ is the magnitude of the pulsar spin angular momentum, and I_1 is its moment of inertia. The fourth term of Equation (13) results from the changing projection of the line of sight onto the orbital plane due to proper motion, with μ and Θ_μ , respectively, the amplitude and position angle of proper motion, and Ω the position angle of the line of nodes (Kopeikin 1996). The final term of Equation (13), involving changes in the Doppler factor D of Equation (1), is caused by the relative line of sight galactic accelerations of the solar system and the binary system.

Table 1
Astrometric and Spin Parameters

Parameter	Value ^a
t_0 (MJD) ^b	52984.0
α (J2000)	19 ^h 15 ^m 27 ^s .99942(3)
δ (J2000)	16°06′27″.3868(5)
μ_α (mas yr ⁻¹)	-1.23(4)
μ_δ (mas yr ⁻¹)	-0.83(4)
f (s ⁻¹)	16.940537785677(3)
\dot{f} (s ⁻²)	-2.4733(1) × 10 ⁻¹⁵
Glitch Parameters	
Glitch epoch (MJD)	52777(2)
Δf (s ⁻¹)	5.49(3) × 10 ⁻¹⁰
$\Delta \dot{f}$ (s ⁻²)	-2.7(1) × 10 ⁻¹⁸

Notes.

^a Figures in parentheses represent formal TEMPO standard errors in the last quoted digit, except for the glitch parameters. The stated uncertainty in glitch epoch results from empirically varying the glitch epoch until $\Delta\chi^2$ corresponds to the 68% confidence level; the quoted uncertainties in the other glitch parameters were derived from their variations as the glitch epoch was varied over the chosen range.

^b This quantity is the epoch of the next six measurements tabulated here.

The above equations demonstrate that measurements of \dot{e} or \dot{x} , along with experimental or theoretical determinations of some of the other quantities appearing therein, can usefully constrain others.

4. RESULTS OF THE FITS

We fitted the parameters discussed above to the full set of TOAs using the TEMPO software as modified by us (see footnote 2). See Tables 1 and 2 for our results and their estimated uncertainties. The uncertainties quoted therein represent the standard errors from the TEMPO fit (except as noted). This convention differs from our previous practice, wherein many uncertainties were instead estimated from fitted parameter variations across multiple reasonable fits. While the old procedure facilitated the incorporation of some systematic uncertainties into the error budget, the more stable recent instrumental configurations appear to minimize such effects.

Some of the fitted parameters shifted by several σ with respect to the values reported in Weisberg et al. (2010). The shifts can all be attributed to the new incorporation of a frequency and time offset for each WAPP observing session, and center frequency in order to account for geodetic precession-induced profile changes (see Section 2), and to our new procedure of fitting for rather than freezing at zero the parameter \dot{x} . The latter procedure also led to a significantly larger uncertainty in the fitted value of γ and in quantities derived therefrom.

The astrometric and spin solutions are listed in Table 1. These are quite similar to those given in Weisberg et al. (2010), except that our longer post-glitch baseline made it clear that the previously discovered glitch at MJD \approx 52770 is better modeled with the addition of a change in spin frequency derivative, $\Delta\dot{f}$. There remains only one known glitch that has a significantly smaller value of $\Delta f/f$ (in globular cluster millisecond PSR B1821-24; Mandal et al. 2009), although several of magnitude

Table 2
Orbital Parameters

Parameter	Value ^a
T_0 (MJD)	52144.90097849(3)
$x \equiv a_1 \sin i$ (s)	2.341776(2)
e	0.6171340(4)
P_b (d)	0.322997448918(3)
ω_0 (deg)	292.54450(8)
$\langle \dot{\omega} \rangle$ (deg yr ⁻¹)	4.226585(4)
γ (ms)	0.004307(4)
\dot{P}_b^{obs}	-2.423(1) × 10 ⁻¹²
$\delta_\theta^{\text{obs}}$	4.0(25) × 10 ⁻⁶
\dot{x}^{obs}	-0.014(9) × 10 ⁻¹²
\dot{e}^{obs} (s ⁻¹)	0.0006(7) × 10 ⁻¹²
Shapiro Gravitational Propagation Delay Parameters	
Damour & Deruelle (1986) Parametrization	
s	0.68 $^{+0.10}_{-0.06}$
r (μs)	9.6 $^{+2.7}_{-3.5}$
Freire & Wex (2010) Parametrization	
ζ	0.38(4)
h_3	0.6(1) × 10 ⁻⁶

Note.

^a Figures in parentheses represent formal TEMPO standard errors in the last quoted digit. The DD Shapiro parameters s and r , which are highly covariant, and their uncertainties were refined through a process illustrated in Figure 2.

similar to the one tabulated here are now known. (See the online Jodrell Bank Pulsar Glitch Catalog⁴; Espinoza et al. 2011). Note that, as with Weisberg et al. (2010), 10 higher-order spin derivatives were also fitted for in order to eliminate the effects of timing noise. Their values are not shown in the Table as they do not correspond to meaningful physical parameters.

Table 2 displays the results of our fit to orbital parameters, including the eight final entries which are fitted here for the first time in this system. Note that the first two of these eight new parameters, namely $\delta_\theta^{\text{obs}}$ and \dot{x}^{obs} , are measured at the marginal 1.5 σ level, while the third, \dot{e}^{obs} , is only an upper limit. All others in this Table, including the new Shapiro terms, are measured with high confidence. In the next sections, we discuss important orbital measurables, including corrections that must be made to some of the observed quantities in order to determine their intrinsic values.

4.1. The Observed and Intrinsic Orbital Period Derivative

The observed orbital period derivative, \dot{P}_b^{obs} , must be corrected by a term, \dot{P}_b^{gal} , resulting from the relative galactic accelerations of the solar system and the binary system (Damour & Taylor 1991), in order to yield the intrinsic derivative, \dot{P}_b^{intr}

$$\dot{P}_b^{\text{intr}} = \dot{P}_b^{\text{obs}} - \dot{P}_b^{\text{gal}}. \quad (15)$$

Using galactic parameters of $R_0 = 8.34 \pm 0.16$ kpc and $\Theta_0 = 240 \pm 8$ km s⁻¹ from Reid et al. (2014), a pulsar distance estimate from Weisberg et al. (2008), and the pulsar proper

⁴ <http://www.jb.man.ac.uk/pulsar/glitches.html>

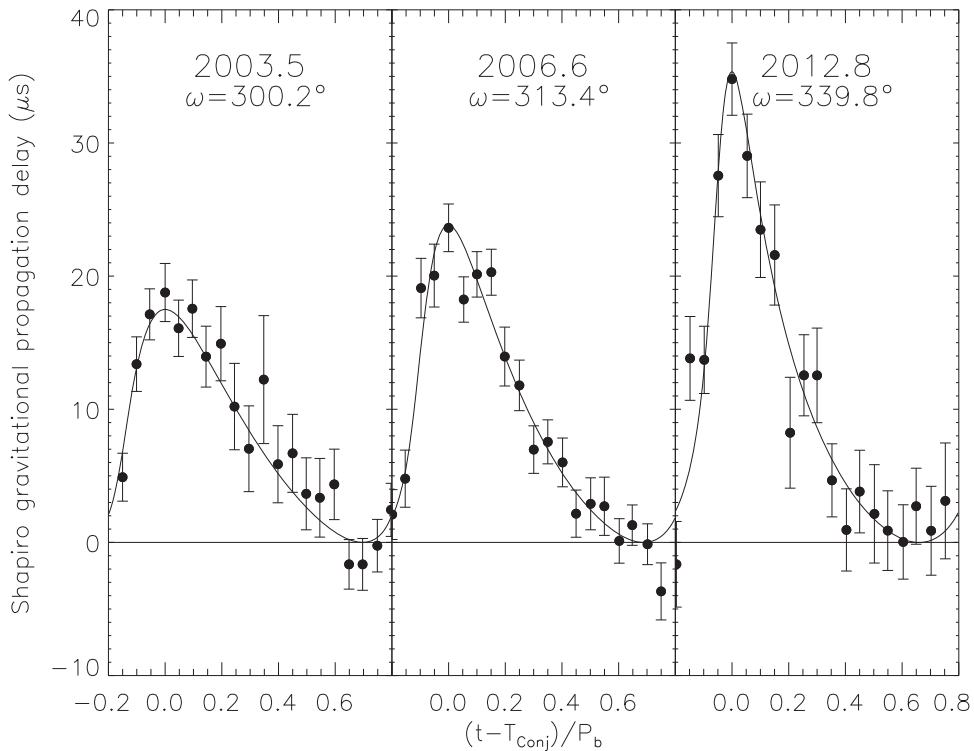


Figure 1. Shapiro gravitational propagation delay variation around the orbit at three epochs. The curve represents the expected delay based on a general relativistic calculation, while the points and their error bars result from combining all residuals to a special fit (see text) near the given epoch into one of 20 orbital time bins. Time is reckoned with respect to T_{Conj} , the epoch of the pulsar’s superior conjunction with the companion. Each curve peaks at that epoch when the pulsar’s earthbound signals plunge most deeply into the companion’s gravitational well. The amplitude and shape of the curves evolve due to relativistic precession of the orbital ellipse, as quantified by the advancing longitude of periastron ω .

motion from Table 1, we find that $\dot{P}_b^{\text{gal}} = -(0.025 \pm 0.004) \times 10^{-12}$. Inserting \dot{P}_b^{obs} from Table 2 into Equation (15), we calculate that $\dot{P}_b^{\text{intr}} = -(2.398 \pm 0.004) \times 10^{-12}$. The uncertainty in this result is dominated by the error in \dot{P}_b^{gal} , which in turn is set principally by the pulsar distance uncertainty. A VLBA parallax campaign on the pulsar currently in progress will hopefully improve these uncertainties.

4.2. First Successful Measurement of the Shapiro Gravitational Propagation Delay Parameters in PSR B1913+16

Due to relativistic precession of the elliptical orbit, the Shapiro delay has recently grown to an amplitude of $\sim 35 \mu\text{s}$ around the orbit, rendering it relatively easy to measure. Figure 1 illustrates the enhancement of the Shapiro delay signal around the orbit over the last dozen years, during which time the WAPP receivers also came into use, thereby increasing our observing bandwidth ten-fold. The curves in Figure 1 illustrate a general relativistic calculation of the expected Shapiro delay variation around the orbit, while the data points are residuals of a TEMPO fit freezing all parameters at their best-fit values, except for the Shapiro parameter r (corresponding in General Relativity to the companion mass). The latter quantity was artificially set to zero to simulate the absence of the Shapiro delay in the fit. The pattern of residuals systematically matches the theoretical expectations for the Shapiro delay.

We have now successfully determined the two Shapiro terms in both the DD and FW parametrizations (see Table 2). While the Shapiro delay has been observed in several other binary pulsar systems, these results mark the first successful detection

of a pair of Shapiro measurables in the PSR B1913+16 system. (The two DD parameters, s and r , had been *jointly* constrained by Taylor & Weisberg (1989). For the ensuing decade, unfavorable orbital geometry rendered its amplitude unmeasurably small, while the last decade has seen both improving orbital geometry and advances in observing instrumentation.) We account for the significant nonlinear covariance of the s and r parameters by estimating their values and uncertainties in Table 2 using a process delineated by Splaver et al. (2002). The procedure is illustrated graphically in Figure 2, which also shows the best-fitting FW Shapiro parameters. (Tighter constraints on the inclination and companion mass can be derived *indirectly* from other measurements. See Section 4.3.)

4.3. Best Determination of Component Masses and Orbital Inclination

The measurement of the first seven quantities in Table 2 enables the precise general relativistic determination of the component masses and orbital inclination. Specifically, our measurements of $\langle \dot{\omega} \rangle$ and γ , along with the Keplerian elements, leave only the two unknowns, $m_{1;\langle \dot{\omega} \rangle, \gamma}$ and $m_{2;\langle \dot{\omega} \rangle, \gamma}$, in the following two general relativistic equations:

$$\begin{aligned} \langle \dot{\omega} \rangle &= 3 G^{2/3} c^{-2} (P_b/2\pi)^{-5/3} \\ &\quad \times (1 - e^2)^{-1} (m_{1;\langle \dot{\omega} \rangle, \gamma} + m_{2;\langle \dot{\omega} \rangle, \gamma})^{2/3} \\ &= 3T_{\odot}^{2/3} (P_b/2\pi)^{-5/3} (1 - e^2)^{-1} \\ &\quad \times \left(\frac{m_{1;\langle \dot{\omega} \rangle, \gamma} + m_{2;\langle \dot{\omega} \rangle, \gamma}}{M_{\odot}} \right)^{2/3}, \end{aligned} \quad (16)$$

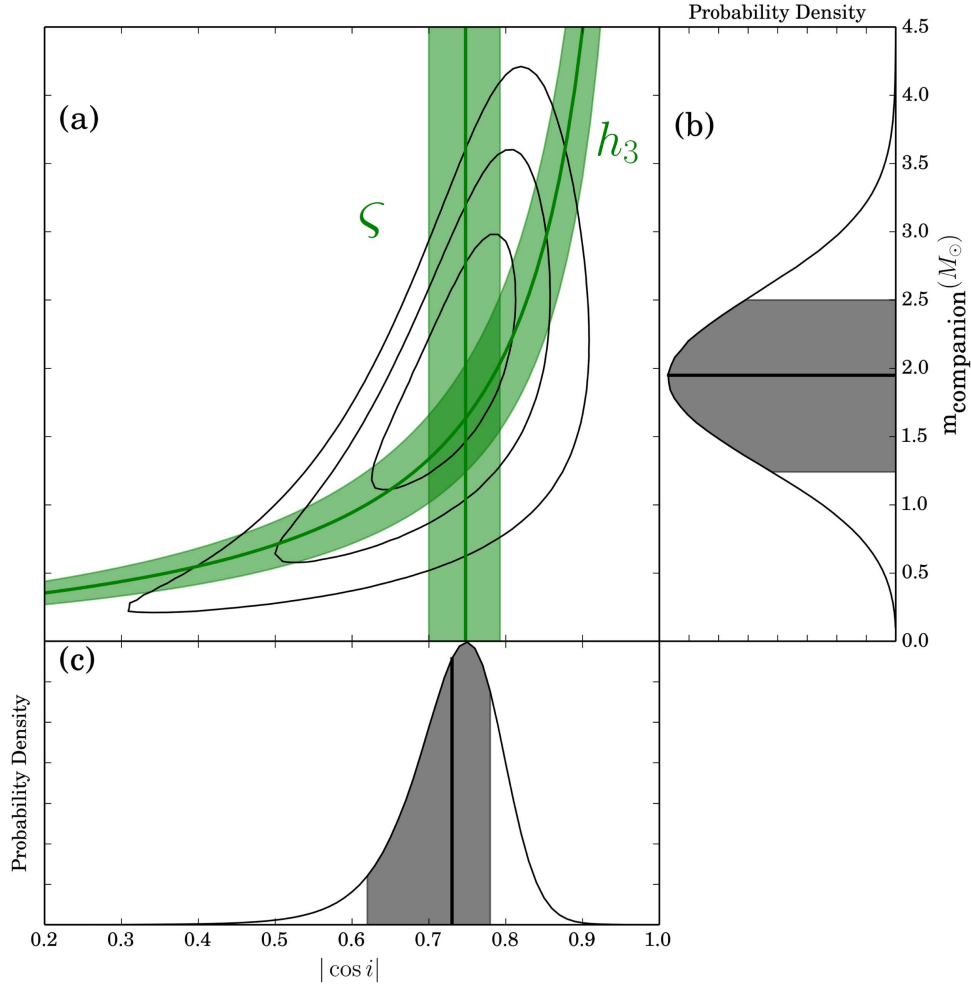


Figure 2. (a) Measured constraints on $|\cos i|$ and m_2 resulting from TEMPO fits for two different parametrizations of the Shapiro gravitational propagation delay within the context of general relativity. The Damour & Deruelle (1986) s and r parameters map directly onto the displayed $|\cos i|$ [$=+\sqrt{1-s^2}$] and m_2 [$=(r/T_\odot)M_\odot$] axes, respectively; the black contours show joint 1, 2, and 3 σ ($\Delta\chi^2 = 2.3, 6.2, 11.8$) confidence limits on those quantities derived from a set of TEMPO fits to a large grid of (fixed) $(|\cos i|, m_2)$. The alternate Freire & Wex (2010) best-fit parameter constraints and their $\pm 1\sigma$ limits are shown in green. Their fitted parameter, ς , transforms directly into the displayed $|\cos i|$ axis (see Equation (4)), whereas their h_3 parameter does not map uniquely onto *either* of the axes (see Equation (5)). The marginal distributions in (b) and (c) result from collapsing the resulting two-dimensional DD probability distribution onto the $|\cos i|$ and m_2 axes, respectively, in which the mean (solid black) and the 1σ bounds (gray region) are displayed, yielding $|\cos i| = 0.73 (+0.05, -0.11)$ and $m_2 = 1.95 (+0.55, -0.71) M_\odot$ (68.3% confidence).

and

$$\begin{aligned}
 \gamma &= G^{2/3} c^{-2} e (P_b/2\pi)^{1/3} m_{2;(\dot{\omega},\gamma)} \\
 &\quad \times (m_{1;(\dot{\omega},\gamma)} + 2m_{2;(\dot{\omega},\gamma)})(m_{1;(\dot{\omega},\gamma)} + m_{2;(\dot{\omega},\gamma)})^{-4/3} \\
 &= T_\odot^{2/3} e (P_b/2\pi)^{1/3} \frac{m_{2;(\dot{\omega},\gamma)}}{M_\odot} \\
 &\quad \times \left(\frac{m_{1;(\dot{\omega},\gamma)} + 2m_{2;(\dot{\omega},\gamma)}}{M_\odot} \right) \left(\frac{m_{1;(\dot{\omega},\gamma)} + m_{2;(\dot{\omega},\gamma)}}{M_\odot} \right)^{-4/3}.
 \end{aligned} \tag{17}$$

Simultaneously solving for the two component masses, we find that $m_{1;(\dot{\omega},\gamma)} = 1.438 \pm 0.001 M_\odot$ and $m_{2;(\dot{\omega},\gamma)} = 1.390 \pm 0.001 M_\odot$. These values agree with WNT within 2σ , while our precision is poorer due to a less-precisely determined γ (see Section 4). Furthermore, Newtonian physics then yields an additional quantity from the derived masses, and our x and P_b measurements, $(\sin i)_{(\dot{\omega},\gamma)} = 0.7327 \pm 0.0004$ (or, equivalently, $|\cos i|_{(\dot{\omega},\gamma)} = 0.6806 \pm 0.0004$). These values are currently

much more precise than the m_2 and $\sin i$ or $|\cos i|$ values determined directly from the Shapiro propagation delay measurements of Section 4.2.

4.4. Toward the First Published Measurement of the Relativistic Orbital Shape Correction, δ_θ , in any System

We have successfully measured the apparent post-Keplerian orbital shape correction term, $\delta_\theta^{\text{obs}}$ (see Table 2). As noted in Section 3.2, this observed value must be corrected for a comparable aberration signal, ϵ_A (see Equation (9)). Geodetic spin-precession modeling of this system should in principle determine the necessary aberration parameters by specifying the spin axis orientation (specifically, its polar angles η and λ) over time (see Equation (7)). However, we find that the currently available pulse shape variation fits (Kramer 1998; Weisberg & Taylor 2002; Clifton & Weisberg 2008) yield inconsistent solutions for these parameters. Consequently, although we have successfully measured $\delta_\theta^{\text{obs}}$, it is not yet

possible to determine $\delta_\theta^{\text{intr}}$ nor to use its measured value as an additional test of relativistic gravitation.

Despite our current inability to *measure* $\delta_\theta^{\text{intr}}$, we can determine its *expected* value, $\delta_\theta^{\text{GR}}$, via a general relativistic calculation (DD; DT92)

$$\begin{aligned} \delta_\theta^{\text{GR}} &= \frac{G^{2/3}}{c^2} \left(\frac{P_b}{2\pi} \right)^{-2/3} (m_1 + m_2)^{-4/3} \\ &\quad \times \left\{ \frac{7}{2} m_1^2 + 6m_1 m_2 + 2m_2^2 \right\} \\ &= T_\odot^{2/3} \left(\frac{P_b}{2\pi} \right)^{-2/3} \left(\frac{m_1 + m_2}{M_\odot} \right)^{-4/3} \\ &\quad \times \left\{ \frac{7}{2} \left(\frac{m_1}{M_\odot} \right)^2 + 6 \left(\frac{m_1 m_2}{M_\odot} \right) + 2 \left(\frac{m_2}{M_\odot} \right)^2 \right\}, \quad (18) \end{aligned}$$

yielding $\delta_\theta^{\text{GR}} = (6.187 \pm 0.001) \times 10^{-6}$. Equation (9) can then be inverted to give the aberration parameter $\epsilon_A = (2.2 \pm 2.5) \times 10^{-6}$. This timing-derived value of ϵ_A will provide a modest consistency check on future geodetic precession modeling.

4.5. Implications of Fits for the First Time-derivatives of e and x

As noted above, Equations (12) and (13) demonstrate that the successful measurement of \dot{e}^{obs} and \dot{x}^{obs} would lead to constraints on other quantities of interest. It is therefore useful to further investigate the various terms composing these equations.

The first (aberration) term of both equations, $d\epsilon_A/dt$, was defined in Equations (10) and (11). However, as discussed in Section 4.4 for ϵ_A , additional progress in understanding the pulsar's spin axis orientation is needed before $d\epsilon_A/dt$ can be confidently determined. Nevertheless, our current geodetic precession modeling suggests that its value is in the $\sim 10^{-15} \text{ s}^{-1}$ range and varies with spin-precessional phase.

4.5.1. Constraints from \dot{e}^{obs}

The second and final term of Equation (12) involves the time evolution of e induced by gravitational wave (GW) emission. For the Equation (12) second term, Peters (1964) shows that this term,

$$\begin{aligned} \left(\frac{\dot{e}}{e} \right)^{\text{GW}} &= -\frac{304}{15} \frac{G^3}{c^5 a_R^4} \mu (m_1 + m_2)^2 \\ &\quad \times (1 - e^2)^{-5/2} \left(1 + \frac{121}{304} e^2 \right) \\ &= -\frac{304}{15} T_\odot^{5/3} \frac{\frac{m_1 m_2}{M_\odot M_\odot}}{\left(\frac{m_1 + m_2}{M_\odot} \right)^{1/3}} \left(\frac{P_b}{2\pi} \right)^{-8/3} \\ &\quad \times (1 - e^2)^{-5/2} \left(1 + \frac{121}{304} e^2 \right) \\ &= -2.9 \times 10^{-17} \text{ s}^{-1}, \quad (19) \end{aligned}$$

with μ as the reduced mass. This term is negligible compared to the expected value of $d\epsilon_A/dt$, except at fortuitous precessional phases where the latter can drop to zero. Consequently, the $d\epsilon_A/dt$ term dominates Equation (12), so that a successful measurement of $(\dot{e}/e)^{\text{obs}}$ would provide a

unique measurement of $d\epsilon_A/dt$. Unfortunately, our fitted value of $(\dot{e}/e)^{\text{obs}}$ is currently not significantly different from zero, although its upper limit is in the 10^{-15} s^{-1} range (see Table 2) expected for $d\epsilon_A/dt$.

4.5.2. Constraints from \dot{x}^{obs}

The second term in Equation (13) delineates the gravitational wave-induced orbital shrinkage rate, which can be evaluated from measurables via

$$\left(\frac{\dot{a}_1}{a_1} \right)^{\text{GW}} = \frac{2}{3} \left(\frac{\dot{P}_b}{P_b} \right)^{\text{GW}} = -5.7 \times 10^{-17} \text{ s}^{-1}. \quad (20)$$

The third (spin-orbit) term of Equation (13) varies approximately sinusoidally on the geodetic precession time-scale with an amplitude of $\sim \pm 3 \times 10^{-15} \text{ s}^{-1}$. Details await a robust determination of geodetic precession parameters (see Equation (14)).

The fourth (Kopeikin 1996) term of Equation (13) has a maximum amplitude⁵ of $\sim 2.3 \times 10^{-16} \text{ s}^{-1}$; while the fifth and final term is

$$-\frac{\dot{D}}{D} = +\frac{\dot{P}_{\text{b,gal}}}{P_b} = -1 \times 10^{-18} \text{ s}^{-1} \quad (21)$$

(see Section 4.1 for details on the calculation of $\dot{P}_{\text{b,gal}}$).

In summary, the first (aberration) and third (spin-orbit) terms dominate Equation (13), so all others may be ignored. However, neither of these two terms is currently accurately determinable. We do have a marginally significant measurement of \dot{x}^{obs} (see Table 2). Consequently, if either of the two terms becomes well-determined in the future, along with an improved value of \dot{x}^{obs} , then the other term will also become accessible. For example, there are two possible paths toward determining the aberrational term: first, additional geodetic precession observations and modeling should better constrain $d\epsilon_A/dt$; and second, additional observations could better determine \dot{e}^{obs} , which, as noted in Section 4.5.1, would then be equivalent to a measurement of $d\epsilon_A/dt$. At this point the spin-orbit term would be calculable, leading to an exciting measurement of the pulsar's moment of inertia, which has important implications for neutron star equations of state (Lattimer & Schutz 2005). With the measurement precision of \dot{x} and \dot{e} improving with time, t , as $t^{-3/2}$, another decade or so of observations is required. Unfortunately, geodetic spin axis precession may cause the pulsar to disappear before that time.

5. TESTS OF RELATIVISTIC GRAVITATION

The determination of seven particular independent quantities suffices to fully determine the dynamics of a binary system within the context of a particular theory of gravitation. For example, the most accurate determination of component masses and orbital inclination in Section 4.3 and of $\delta_\theta^{\text{GR}}$ in Section 4.4 depend upon subsets of the first seven measurements listed in Table 2.

Consequently, any additional measurement would constitute an independent test of relativistic gravitation under strong-field conditions. In the following two sections, we delineate relativistic gravitational tests via measurements of gravitational radiation emission and of the Shapiro gravitational propagation delay, respectively.

⁵ The exact value depends on the unknown alignment on the sky of the line of nodes.

5.1. Gravitational Radiation Emission and \dot{P}_b

Gravitational radiation emission should cause the orbit to decay as orbital energy is radiated away. The quantity \dot{P}_b^{GR} is the resulting orbital period derivative expected from a general relativistic calculation of this phenomenon (Peters & Mathews 1963):

$$\begin{aligned} \dot{P}_b^{\text{GR}} &= -\frac{192 \pi G^{5/3}}{5 c^5} \left(\frac{P_b}{2\pi}\right)^{-5/3} \\ &\quad \times \left(1 + \frac{73}{24}e^2 + \frac{37}{96}e^4\right) (1 - e^2)^{-7/2} \\ &\quad \times m_1 m_2 (m_1 + m_2)^{-1/3} \\ &= -\frac{192 \pi}{5} T_\odot^{5/3} \left(\frac{P_b}{2\pi}\right)^{-5/3} \\ &\quad \times \left(1 + \frac{73}{24}e^2 + \frac{37}{96}e^4\right) (1 - e^2)^{-7/2} \\ &\quad \times \left(\frac{m_1}{M_\odot}\right) \left(\frac{m_2}{M_\odot}\right) \left(\frac{m_1 + m_2}{M_\odot}\right)^{-1/3}. \end{aligned} \quad (22)$$

Inserting our measured and derived values and their uncertainties into Equation (22)⁶, we find that $\dot{P}_b^{\text{GR}} = (-2.40263 \pm 0.00005) \times 10^{-12}$. To verify our estimate of the error in \dot{P}_b^{GR} that was derived via propagation of uncertainty, we also employed a Monte-Carlo method with Cholesky decomposition of the covariance matrix. In this fashion, we simulated the joint normal distribution of measured parameters $\{\gamma, \dot{\omega}, P_b, e\}$, and then constructed a histogram of 1,000,000 derived \dot{P}_b^{GR} and inferred the uncertainty therefrom.

Consequently, we find that

$$\begin{aligned} \frac{\dot{P}_b^{\text{intr}}}{\dot{P}_b^{\text{GR}}} &= \frac{(-2.398 \pm 0.004) \times 10^{-12}}{(-2.40263 \pm 0.00005) \times 10^{-12}} \\ &= 0.9983 \pm 0.0016. \end{aligned} \quad (23)$$

This result demonstrates that the system is losing energy to gravitational radiation within $\sim 1\sigma$ of the rate predicted by general relativity (see also Figure 3 and the red curve in Figure 4). The above number represents a significant improvement over the value determined by WNT, 0.997 ± 0.002 , which represented a 1.8σ discrepancy between our measurements and general relativity. Interestingly, the new galactic parameters of Reid et al. (2014) are the principal reason for the improvement (via a change in \dot{P}_b^{gal}), while our measured values themselves changed little.

In addition to confirming general relativistic radiation damping at this level, our result rules out large parameter spaces in plausible scalar–tensor theories of gravity. In recent years, however, other pulsars in neutron-star–white-dwarf binary systems have overtaken PSR B1913+16 in constraining these alternatives (Freire et al. 2012).

DD92 point out that this test is a “mixed” strong-field probe in that it involves a combination of radiative effects (via \dot{P}_b^{obs}) and quasi-static phenomena (through $\langle \dot{\omega} \rangle$ and γ , whose values are needed in order to make a prediction of the expected \dot{P}_b^{GR}). Consequently, additional tests, such as those described in the

next section, that probe different aspects of strong-field gravitation are also useful for constraining viable alternatives to general relativity.

5.2. Shapiro Gravitational Propagation Delay

Each of the two newly measured Shapiro parameters represents another independent test of relativistic gravitation. As with the \dot{P}_b test of Section 5.1, the Shapiro tests also require the complementary measurement of $\langle \dot{\omega} \rangle$ and γ in order to make a testable prediction for the value of the Shapiro parameters. In this case, unlike the \dot{P}_b test, all of the post-Keplerian quantities probe quasi-static phenomena in strong fields. While Shapiro parameters have already been measured in several other binary systems, it is especially useful to constrain theories via systems such as this one and PSRs B1534+12, and J0737-3039A where at least three “excess” post-Keplerian parameters beyond $\langle \dot{\omega} \rangle$ and γ (one gravitational radiation parameter and two Shapiro quantities) are measurable. Although the precision of the binary pulsar Shapiro parameter measurements is well below their measurement precision in the weak solar gravitational field, it is this simultaneous determination of several parameters in strong-field conditions in each of these binary pulsar systems that leads to the important constraints on relativistic theories of gravitation.

In the DD formulation of the Shapiro delay within general relativity, the Shapiro measurables s and r map directly onto $\sin i$ and m_2 , respectively. Hence we can test general relativity by comparing the Shapiro determination of $\sin i$ ($\equiv s$) with that determined from $\langle \dot{\omega} \rangle$ and γ (called $\sin i_{\langle \dot{\omega}, \gamma \rangle}$; see Section 4.3):

$$\frac{s}{\sin i_{\langle \dot{\omega}, \gamma \rangle}} = \frac{0.68^{+0.10}_{-0.06}}{0.7327 \pm 0.0004} = 0.93^{+0.14}_{-0.07}. \quad (24)$$

Similarly, we can test general relativity by comparing the Shapiro determination of m_2 ($\equiv r M_\odot / T_\odot$) with that determined from $\langle \dot{\omega} \rangle$ and γ

$$\frac{r M_\odot / T_\odot}{m_{2; \langle \dot{\omega}, \gamma \rangle}} = \frac{(1.95^{+0.55}_{-0.71}) M_\odot}{(1.390 \pm 0.001) M_\odot} = 1.40^{+0.40}_{-0.51}. \quad (25)$$

The consistency (albeit with a rather low level of precision) of these Shapiro determinations of $\sin i$ and m_2 with those measured via the other post-Keplerian terms, and hence their confirmation of general relativity, is also graphically depicted in Figure 4. The Shapiro terms have also been measured in several other binary pulsar systems with higher precision, and have also been shown to be in agreement with general relativity.

6. CONCLUSIONS

We report here on the measurements and relativistic analyses of 9309 TOAs in over 30 years of high-quality Arecibo data on binary pulsar PSR B1913+16. We fitted for a number of previously unmeasurable parameters for the first time in this system (and in one case, for the first time anywhere), which enabled us to significantly advance our relativistic analyses of the system. We provide our newest measurements or derivations of all relevant physical quantities of the binary system, with the exception of Ω , the position angle of the line of nodes. We rigorously ascertained the uncertainties in the fitted and derived parameters. Having fully characterized the system, we proceeded to use it in several tests of general relativity in strong-field conditions.

We have measured a gravitational radiation-induced orbital period decrease whose rate agrees with the general relativistic

⁶ This value may also be calculated directly from the first seven orbital measurables in Table 2 alone and without the use of derived quantities such as the masses (DT91).

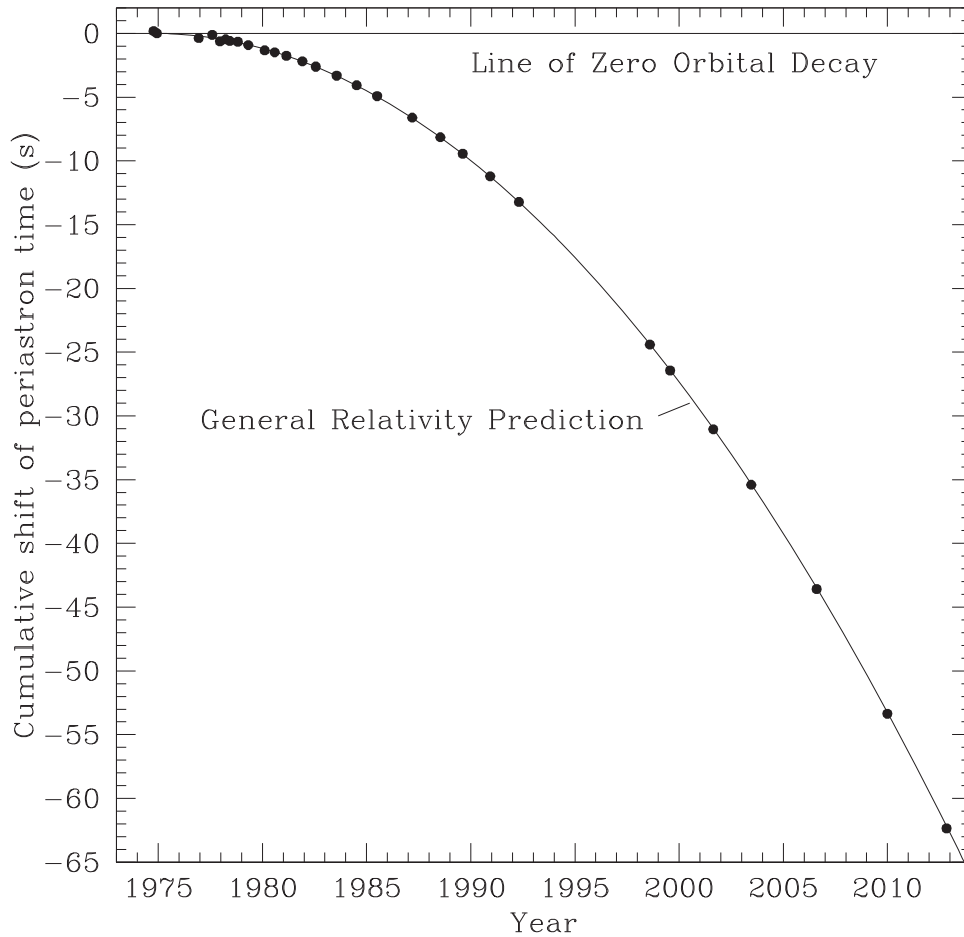


Figure 3. Orbital decay of PSR B1913+16 as a function of time. The curve represents the orbital phase shift expected from gravitational wave emission according to General Relativity. The points, with error bars too small to show, represent our measurements.

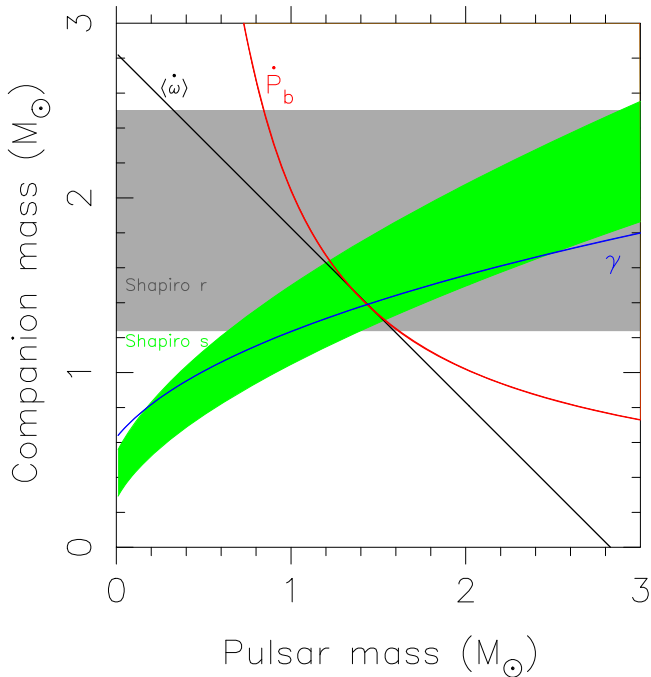


Figure 4. Constraints on the masses of the pulsar and the companion as a function of five post-Keplerian measurables, within the context of General Relativity. The width of each curve represents $\pm 1\sigma$ error bounds. The mutual near-intersection of all curves illustrates the agreement of our observations with general relativity in the strong-field conditions at the binary system.

expectation to within $\sim 1\sigma$, which is closer than found by WNT, largely as a result of an improved galactic correction resulting from more accurate galactic parameters (Reid et al. 2014).

Similar orbital decay tests have now been performed with several other binary pulsars (see Table 3 for published measurements of $\dot{P}_b^{\text{intr}}/\dot{P}_b^{\text{GR}}$). The orbital decays of PSRs J0348+0432, J0737-3039, J1141-4565, J1738+0333, J1906+0746, B1913+16, and B2127+11C all exhibit agreement between observation and general relativity to within (or very close to) the authors’ stated uncertainties. PSR B1913+16 currently has the most precise determination, and interferometric parallax measurements currently in progress will hopefully further tighten the precision.

Among the other two, PSR B1534+12 and PSR J1756-2251, various systematic effects such as an incorrect distance in the galactic acceleration correction may explain the small observed discrepancies, although it is possible that an incompleteness of general relativity or some unknown physical effect is responsible. See the work of Ferdman et al. (2014) for an especially thorough description of the most significant deviation of the orbital decay rate from the general relativistic prediction, found in PSR J1756-2251.

Our new (for this system) measurements of Shapiro gravitational propagation delay parameters represent two additional tests of relativistic gravitation, and are fully consistent with general relativity, although their relative precision is currently far

Table 3
Comparison of Gravitational Radiation-induced Orbital Decay with GR Prediction in Binary Pulsars

PSR	$\dot{P}_b^{\text{intr}}/\dot{P}_b^{\text{GR}}$	References
J0348+0432	1.05 ± 0.18	Antoniadis et al. (2013)
J0737-3039	1.003 ± 0.014	Kramer et al. (2006)
J1141-6545	1.04 ± 0.06	Bhat et al. (2008)
B1534+12	0.91 ± 0.06	Stairs et al. (2002)
J1738+0333	0.94 ± 0.13	Freire et al. (2012)
J1756-2251	1.08 ± 0.03	Ferdman et al. (2014)
J1906+0746	1.01 ± 0.05^a	van Leeuwen et al. (2015)
B1913+16	0.9983 ± 0.0016	This work
B2127+11C	1.00 ± 0.03	Jacoby et al. (2006)

Note.

^a Assumes negligible proper motion.

lower than the orbital decay test. This binary now joins several other systems, including PSRs J0737-3039A, B1534+12, and J1756-2251, with each providing at least three independent tests of relativistic, strong-field gravitation.

We have also marginally measured the orbital shape parameter δ_θ for the first time anywhere, but its intrinsic value is corrupted by a comparable, undetermined aberration delay. Future geodetic spin-orbit precession measurements should lead to an accurate characterization of the aberration and then an additional relativistic gravitational test via the comparison of the aberration-corrected $\delta_\theta^{\text{intr}}$ with $\delta_\theta^{\text{GR}}$.

In addition, we fitted for the time derivative of orbital eccentricity, e , and the projected semimajor axis of the pulsar orbit, x , and we achieved an upper limit on the former and a marginal detection of the latter. We discussed and quantified the various physical phenomena that can contribute to these parameters. Unless the pulsar disappears in the next few years due to geodetic spin axis precession, future timing observations should better define these quantities, allowing for a determination of the pulsar's moment of inertia, I_1 .

We have placed online (see footnote 2) a subroutine and modifications to the TEMPO TOA fitting software, which codes the Freire & Wex (2010) parametrization of the Shapiro delay for high-eccentricity binary pulsars such as the PSR B1913+16 system. The TEMPO input files and TOAs upon which these analyses are based are available in a .tar.gz package published with this paper and in a persistent repository <http://dx.doi.org/10.5281/zenodo.54764> and with the article preprint <http://arxiv.org/e-print/1606.02744v1>.

Much of this experiment was pioneered by J.H. Taylor, to whom we owe our deepest thanks. D.J. Nice assisted with observing and analyses, and A.A. Chael assisted in developing the FW analysis package. The authors gratefully acknowledge financial support from the US National Science Foundation. The Arecibo Observatory is operated by SRI International under a cooperative agreement with the National Science Foundation (AST-1100968), and in alliance with Ana G. Mendez-Universidad Metropolitana, and the Universities Space Research Association.

Facility: Arecibo.

REFERENCES

- Antoniadis, J., Freire, P. C. C., Wex, N., et al. 2013, *Sci*, **340**, 448
 Bhat, N. D. R., Bailes, M., & Verbiest, J. P. W. 2008, *PhRvD*, **77**, 124017
 Clifton, T., & Weisberg, J. M. 2008, *ApJ*, **679**, 687
 Damour, T., & Deruelle, N. 1986, *AnIHP*, **44**, 263 (DD)
 Damour, T., & Taylor, J. H. 1991, *ApJ*, **366**, 501 (DT91)
 Damour, T., & Taylor, J. H. 1992, *PhRvD*, **45**, 1840 (DT92)
 Demorest, P. B., Ferdman, R. D., Gonzalez, M. E., et al. 2013, *ApJ*, **762**, 94
 Espinoza, C. M., Lyne, A. G., Stappers, B. W., & Kramer, M. 2011, *MNRAS*, **414**, 1679
 Ferdman, R. D., Stairs, I. H., Kramer, M., et al. 2014, *MNRAS*, **443**, 2183
 Freire, P. C. C., & Wex, N. 2010, *MNRAS*, **409**, 199 (FW)
 Freire, P. C. C., Wex, N., Esposito-Farèse, G., et al. 2012, *MNRAS*, **423**, 3328
 Hulse, R. A., & Taylor, J. H. 1975, *ApJL*, **195**, L51
 Jacoby, B. A., Cameron, P. B., Jenet, F. A., et al. 2006, *ApJL*, **644**, L113
 Kopeikin, S. M. 1996, *ApJL*, **467**, L93
 Kramer, M. 1998, *ApJ*, **509**, 856
 Kramer, M., Stairs, I. H., Manchester, R. N., et al. 2006, *Sci*, **314**, 97
 Lattimer, J. M., & Schutz, B. F. 2005, *ApJ*, **629**, 979
 Lorimer, D. R., & Kramer, M. 2004, *Handbook of Pulsar Astronomy*, Vol. 4 (Cambridge: Cambridge Univ. Press), 229
 Mandal, R. D. R., Konar, S., Dey, M., & Dey, J. 2009, *MNRAS*, **399**, 822
 Peters, P. C. 1964, *PhRv*, **136**, 1224
 Peters, P. C., & Mathews, J. 1963, *PhRv*, **131**, 435
 Reid, M. J., Menten, K. M., Brunthaler, A., et al. 2014, *ApJ*, **783**, 130
 Shapiro, I. I. 1964, *PhRvL*, **13**, 789
 Splaver, E. M., Nice, D. J., Arzoumanian, Z., et al. 2002, *ApJ*, **581**, 509
 Stairs, I. H., Thorsett, S. E., Taylor, J. H., & Wolszczan, A. 2002, *ApJ*, **581**, 501
 Taylor, J. H., & Weisberg, J. M. 1982, *ApJ*, **253**, 908
 Taylor, J. H., & Weisberg, J. M. 1989, *ApJ*, **345**, 434
 van Leeuwen, J., Kasian, L., Stairs, I. H., et al. 2015, *ApJ*, **798**, 118
 Weisberg, J. M., Nice, D. J., & Taylor, J. H. 2010, *ApJ*, **722**, 1030 (WNT)
 Weisberg, J. M., Romani, R. W., & Taylor, J. H. 1989, *ApJ*, **347**, 1030
 Weisberg, J. M., Stanimirović, S., Xilouris, K., et al. 2008, *ApJ*, **674**, 286
 Weisberg, J. M., & Taylor, J. H. 1981, *GReGr*, **13**, 1
 Weisberg, J. M., & Taylor, J. H. 2002, *ApJ*, **576**, 942
 You, X. P., Hobbs, G., Coles, W. A., et al. 2007, *MNRAS*, **378**, 493